RESEARCH ARTICLE

Prediction of a multifunctional hexagonal Fe_2O_3 monolayer with chiral antiferromagnetism and piezoelectricity

Qi Wang[1], Junyuan Wang[1], Xu Yan[1,2,*], Guochun Yang[1,#]

[1]State Key Laboratory of Metastable Materials Science & Technology and Hebei Key Laboratory of Microstructural Material Physics, School of Science, Yanshan University, Qinhuangdao 066004, China

[2]College of Physics and Hebei Advanced Thin Films Laboratory, Hebei Normal University, Shijiazhuang 050024, China

Corresponding authors. E-mail: [*]xuyan980504@163.com, [#]yanggc468@nenu.edu.cn

Received December 17, 2025; accepted March 27, 2026

Supporting Information

Computational Details

First-principles calculations were performed using the Vienna Ab initio Simulation Package (VASP) [1,2] within the framework of density functional theory (DFT) [3] and the projector augmented wave (PAW) [4] method. The Perdew-Burke-Ernzerhof (PBE) [5] exchange-correlation functional within the generalized gradient approximation (GGA) was employed. To account for the strong electron correlation of Fe-3*d* electrons, an effective Hubbard U parameter of 7.89 eV was adopted. The U_{eff} value was determined using two criteria: (1) the PBE+U band gap should be closest to the HSE06 band gap, and (2) the Fe local magnetic moment should be close to the expected 5 μ_B for Fe^{3+}. Specifically, the HSE06 band gap is 3.55 eV, while the PBE+U band gap at $U_{eff} = 7.89$ eV is 3.10 eV. At $U_{eff} = 7.89$ eV, the Fe magnetic moment is 4.56 μ_B, which is close to 5 μ_B and consistent with Fe^{3+}. Therefore, $U_{eff} = 7.89$ eV was selected in this work. This value was determined by calibrating the electronic bandgap against calculations using the HSE06 [6] hybrid functional while also ensuring a reasonable magnetic moment (Fig. S7).

The plane-wave energy cutoff was set to 450 eV. A vacuum layer larger than 15 Å was used to eliminate spurious interactions between periodic images. Lattice constants and atomic positions were fully relaxed until the forces on each atom were less than 0.01 eV/Å and the energy tolerance was below 10^{-6} eV. Spin-orbit coupling (SOC) was included. Phonon dispersion spectra of Fe_2O_3 monolayers with different magnetic configurations were calculated using the PHONOPY code [7] based on density functional perturbation theory (DFPT) to confirm their dynamical stability. Thermal stability at 300 K was further assessed via ab initio molecular dynamics (AIMD) simulations [8]. Piezoelectric strain tensors were calculated using DFPT [9].

Magnetic properties were investigated through Monte Carlo (MC) simulations performed with the MTC code [10]. The MC simulations, based on the Heisenberg model, were performed using a 20 × 20 supercell. In each simulation, the system was first equilibrated over 700,000 relaxation steps, followed by 900,000 sampling steps, resulting in a total of 1,600,000 steps. Spin updates were carried out using the Metropolis algorithm, where each spin undergoes a random trial rotation and is accepted according to the Metropolis criterion based on the energy change. By inspecting the magnetic moment snapshots at different temperatures, the Néel temperature (T_N) was identified as approximately 40 K, where the chiral antiferromagnetic order disappears. The Young's modulus and Poisson's ratio are derived from the in-plane Young's modulus $Y(\theta)$ and Poisson's ratio $v(\theta)$ as follows

$$Y(\theta)=\frac{C_{11}C_{22} - C_{12}^2}{C_{11}s^4 + C_{22}c^4 + As^2c^2}, \tag{1}$$

$$v(\theta)=\frac{Bc^2s^2 - C_{12}(c^4 + s^4)}{C_{11}s^4 + C_{22}c^4 + As^2c^2}, \tag{2}$$

where

$$s = \sin\theta, \tag{3}$$

$$c = \cos\theta, \tag{4}$$

$$A = (C_{11}C_{22} - C_{12}^2) / C_{66} - 2C_{12}, \tag{5}$$

$$B = C_{11} + C_{22} - (C_{11}C_{22} - C_{12}^2) / C_{66}. \tag{6}$$

The three-dimensional (3D) magnetic anisotropy energy (MAE) surface is obtained by performing a series of fully relativistic self-consistent field (SCF) calculations within density functional theory, explicitly including spin-orbit coupling. For each orientation of the spin spiral plane, characterized by the polar angle θ and azimuthal angle φ, the entire non-collinear magnetic texture (a 120° antiferromagnetic order) is rigidly rotated as a whole, preserving the relative angles between individual magnetic moments. Total energies are obtained from self-consistent calculations with the magnetic moments constrained to the prescribed directions. The energy zero is set to the total energy corresponding to the spin spiral lying in the *xy*-plane ($\theta = 90°$). The resulting energy differences $\Delta E(\theta, \varphi) = E(\theta, \varphi) - E(\theta = 90°)$ are mapped onto a spherical surface to visualize the MAE as a function of the spin-spiral-plane orientation.

Supplementary Figures

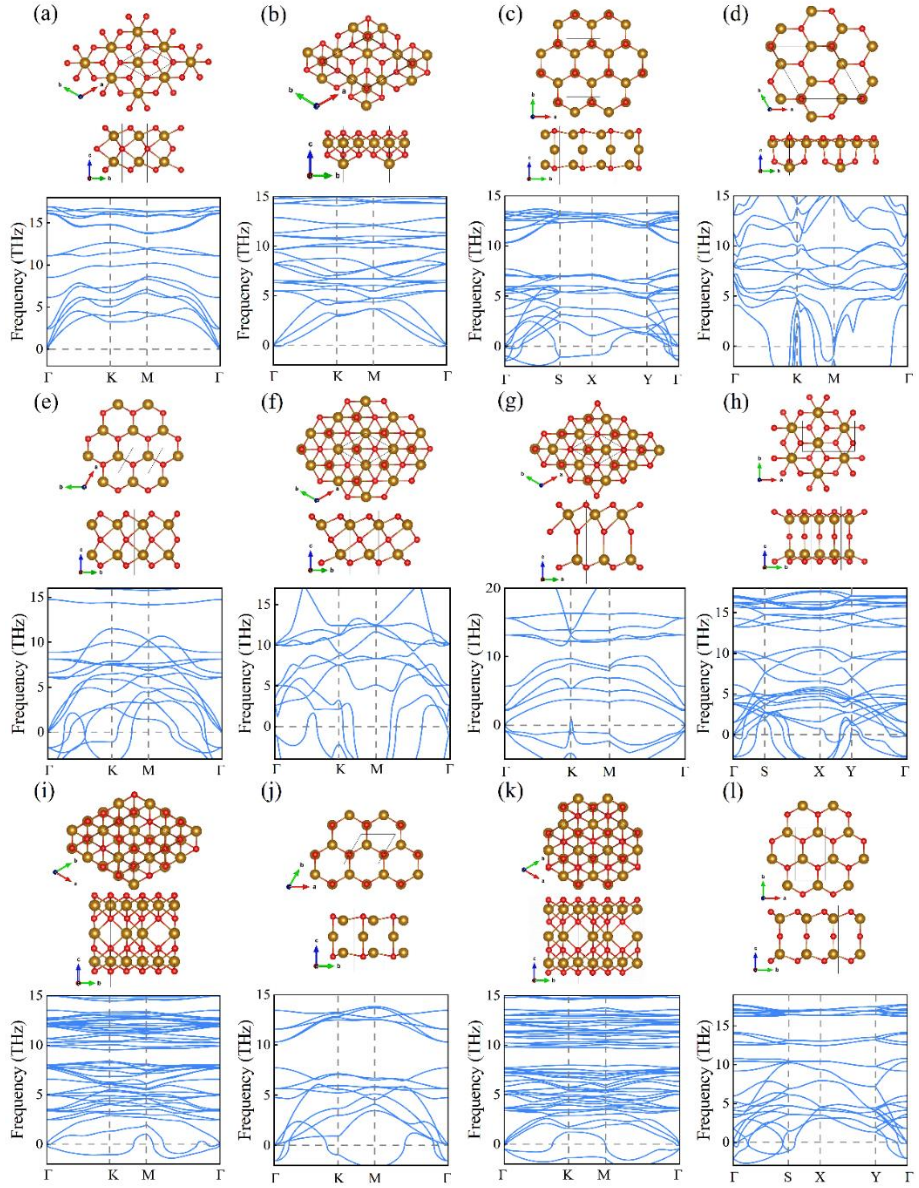

Fig. S1 Twelve candidate hexagonal configurations (a–l) of Fe_2O_3 monolayers were considered. The upper panels show the atomic structures, while the lower panels present their corresponding phonon spectra. Among these configurations, only two are dynamically stable, and the total energy of structure (a) is 0.33 eV/f.u. lower than that of structure (b).

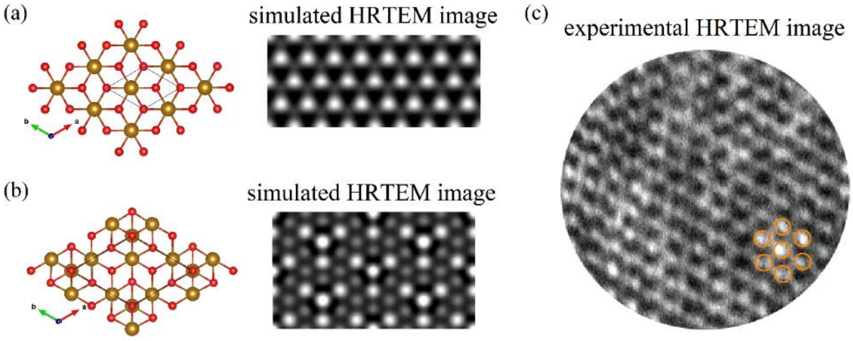

Fig. S2 (a) and (b) Simulated HRTEM images for the two dynamically stable configurations identified in Fig. S1, along with the (c) experimental HRTEM image for comparison [11]. The simulated image in (a) exhibits a significantly better agreement with the experimental result. Moreover, the total energy of structure (a) is 0.33 eV/f.u. lower than that of structure (b). These findings collectively indicate that structure (a) is the most plausible candidate configuration for monolayer Fe_2O_3.

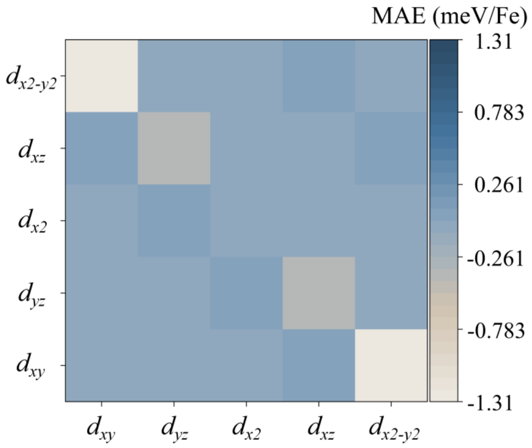

Fig. S3 Orbital-decomposed MAE contributions of the Fe_2O_3 monolayer.

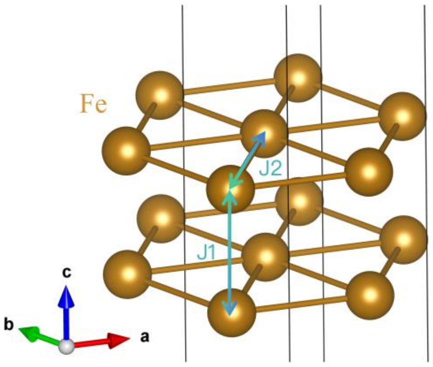

Fig. S4 Schematic illustration of exchange paths.

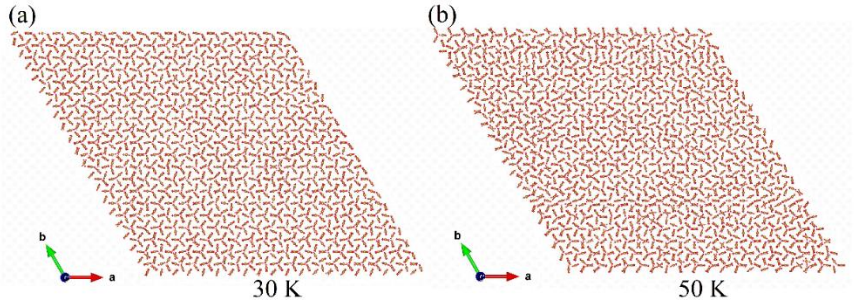

Fig. S5 Real-space distribution of magnetic moments at (a) 30 K and (b) 50 K.

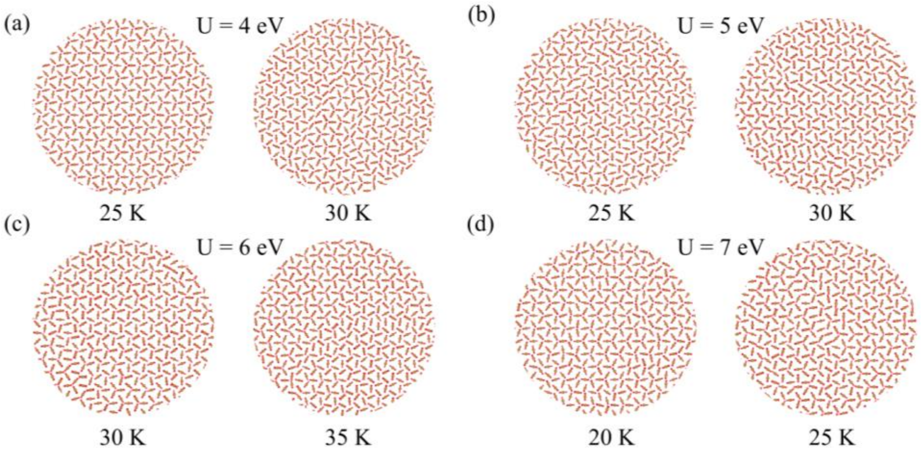

Fig. S6 Magnetic moment snapshots of the Fe_2O_3 monolayer obtained from Monte Carlo simulations using the PBE+U method across U values ranging from 4 to 7 eV. By inspecting the evolution of the spin configurations with temperature, the chiral 120° antiferromagnetic order is observed to break down near the critical temperature, where adjacent magnetic moments deviate from the 120° arrangement and tend to align more parallel. The Néel temperature (T_N) is thus estimated as the temperature interval where this transition occurs, providing an approximate range for the magnetic phase transition.

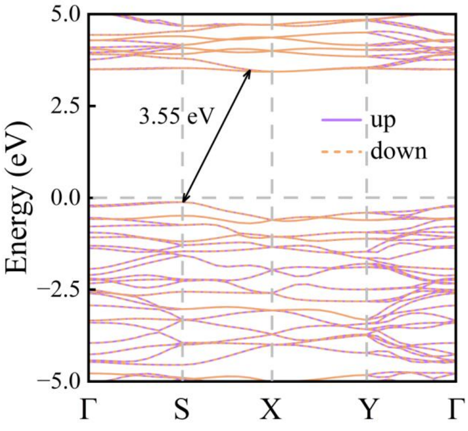

Fig. S7 Band structure of the Fe_2O_3 monolayer at HSE06 level.

Supplementary Tables

Table S1 Structural information of the Fe_2O_3 monolayer.

	Lattice Parameters (Å, °)	**Atoms**	**Wyckoff Positions (fractional)**		
			x	***y***	***z***
Fe_2O_3	*a* = 3.0084	O (2*i*)	−0.33333	1.33333	−0.42751
	b = 3.0084	O (1*d*)	−0.66667	0.66667	−0.50000
	c = 30.0000	Fe (2*g*)	−2.00000	1.00000	−0.45260
	$\alpha = \beta = 90.0000$				
	$\gamma = 120.0000$				

Table S2 Magnetic anisotropy energy of the Fe_2O_3 monolayer as a function of the Hubbard U parameter. The magnetocrystalline anisotropy (SOC-MAE) and shape anisotropy (Shape-MAE) contributions are shown for U_{eff} values ranging from 4.00 to 7.89 eV.

U (eV)	**4.00**	**5.00**	**6.00**	**7.00**	**7.89**
SOC-MAE (meV/Fe)	3.32	3.49	3.60	3.67	3.88
Shape-MAE (meV/Fe)	0.384	0.386	0.387	0.389	0.394

Table S3 Hubbard U dependence of the exchange parameters (J_1, J_2) and Néel temperature (T_N) for the Fe_2O_3 monolayer over U_{eff} = 4.0-7.89 eV.

U (eV)	**4**	**5**	**6**	**7**	**7.89**
J_1 (meV)	10.52	9.43	8.33	7.17	0.84
J_2 (meV)	−7.17	−5.97	−4.94	−4.03	−2.80
T_N (K)	25	25	30	20	40

Table S4 Energies in eV/f.u. of the Fe_2O_3 monolayer with six considered magnetic configurations under −6%~2% biaxial strain.

Strain (%)	**FM**	**AFM1**	**AFM2**	**FIM1**	**FIM2**	**chiral AFM**
−6	−30.55	−30.62	−30.75	−30.70	−30.78	−30.79
−4	−30.89	−30.96	−31.07	−31.10	−31.09	−31.11
−2	−31.10	−31.17	−31.26	−31.22	−31.29	−31.30
0	−31.19	−31.26	−31.34	−31.30	−31.36	−31.37
2	−31.16	−31.23	−31.31	−31.27	−31.33	−31.34

References

1. J. F. G. Kresse, Efficient iterative schemes for ab initio total-energy calculations using a plane-wave basis set, *Phys. Rev. B* 54(16), 11169 (1996).
2. J. F. G. Kresse, Efficiency of ab-initio total energy calculations for metals and semiconductors using a plane-wave basis set, *Comput. Mater. Sci.* 6, 15 (1996).

3. W. Kohn and L. J. Sham, Self-Consistent Equations Including Exchange and Correlation Effects, *Phys. Rev.* 140(4A), A1133 (1965).
4. D. J. G. Kresse, From ultrasoft pseudopotentials to the projector augmented-wave method, *Phys. Rev. B* 59(3), 1758 (1999).
5. J. P. Perdew, K. Burke, and M. Ernzerhof, Generalized gradient approximation made simple, *Phys. Rev. Lett.* 77(18), 3865 (1996).
6. G. E. S. Jochen Heyd, Matthias Ernzerhof, Hybrid functionals based on a screened Coulomb potential, *J. Chem. Phys.* 118(18), 8207 (2003).
7. A. Togo and I. Tanaka, First principles phonon calculations in materials science, *Scr. Mater.* 108, 1(2015).
8. G. J. Martyna, M. L. Klein, and M. Tuckerman, Nosé–Hoover chains: The canonical ensemble via continuous dynamics, *J. Chem. Phys.* 97(4), 2635 (1992).
9. X. Wu, D. Vanderbilt, and D. R. Hamann, Systematic treatment of displacements, strains, and electric fields in density-functional perturbation theory, *Phys. Rev. B* 72(3), 035105 (2005).
10. Y. Zhang, B. Wang, Y. Guo, Q. Li, and J. Wang, A universal framework for metropolis Monte Carlo simulation of magnetic Curie temperature, *Comput. Mater. Sci.* 197 (2021).
11. B. Y. Zhang *et al.*, Hexagonal metal oxide monolayers derived from the metal–gas interface, *Nat. Mater.* 20(8), 1073 (2021).